

A Novel Spoke-Type Asymmetric Rotor Interior Permanent Magnet Machine

Yang Xiao , Z. Q. Zhu , Fellow, IEEE, Geraint Wyn Jewell , Jintao Chen, Senior Member, IEEE, Di Wu, and Liming Gong

Abstract—This article proposes a novel spoke-type asymmetric interior permanent magnet (AIPM) rotor topology that employs an additional asymmetric flux barrier in each pole of interior permanent magnet (IPM) synchronous machines for torque density enhancement and torque pulsating suppression without introducing any extra cost. The proposed AIPM-I machine, an existing spoke-type AIPM-II machine with asymmetric rotor profile, and a conventional spoke-type IPM machine are designed and optimized with the same 12-slot/8-pole stator with nonoverlapping windings as well as the same rotor diameter and PM dimensions. The effect of asymmetric flux barrier dimensions on the proposed AIPM-I machine is investigated with particular emphasis on torque characteristics. The electromagnetic performance and rotor mechanical strength of final optimal designs of three machines are compared. It confirms that the proposed AIPM-I machine can achieve significant torque enhancement and torque ripple reduction across the wide current range while also showing significantly smaller cogging torque at open-circuit condition, compared with both existing AIPM-II and conventional IPM machines. Finally, a prototype of the proposed AIPM-I machine has been manufactured and measured for validation.

Index Terms—Asymmetric rotor, flux barrier, interior permanent magnet (IPM), spoke-type permanent magnet (PM), torque ripple.

I. INTRODUCTION

PERMANENT magnet (PM) synchronous machines have been increasingly employed in many industrial applications and electric transportation propulsion systems due to advantages of superior torque density, high efficiency, and high power factor [1], [2]. Among PM machines, interior PM (IPM) synchronous machines whose PMs are buried inside the rotor core lamination

Manuscript received March 29, 2021; revised June 12, 2021; accepted July 18, 2021. Date of publication July 26, 2021; date of current version September 16, 2021. Paper 2021-EMC-0363.R1, presented at the 2020 IEEE Energy Conversion Congress and Exposition, Detroit, MI, USA, Oct. 11–15, and approved for publication in the IEEE TRANSACTIONS ON INDUSTRY APPLICATIONS by the Electric Machines Committee of the IEEE Industry Applications Society. (Corresponding author: Z. Q. Zhu.)

Yang Xiao, Z. Q. Zhu, and Geraint Wyn Jewell are with the Department of Electronic and Electrical Engineering, University of Sheffield, S1 3JD Sheffield, U.K. (e-mail: yxiao23@sheffield.ac.uk; z.q.zhu@sheffield.ac.uk; g.jewell@sheffield.ac.uk).

Jintao Chen, Di Wu, and Liming Gong are with the Midea Shanghai Motors and Drives Research Center, Shanghai 201203, China (e-mail: chenjintao@welling.com.cn; wudi9@welling.com.cn; gongliming@midea.com).

Color versions of one or more figures in this article are available at <https://doi.org/10.1109/TIA.2021.3099452>.

Digital Object Identifier 10.1109/TIA.2021.3099452

rather than placed on the rotor surface are preferred in applications that require high torque density per PM volume, strong mechanical robustness, and wide speed range [3]–[6].

Rotor topologies of IPM machines, in terms of PM configuration and rotor core geometry, are critical for machine performance. In literature, many different IPM rotor topologies have been reported, i.e., Bar-shape, V-shape, Delta-shape, Double-V shape PM structures [7]–[12], multilayer designs [13], [14], and spoke-type PM topologies [15]. Among these designs, spoke-type IPM machines are competitive candidates for some applications due to simple rotor structure with only one piece of PM per pole and with potential flux focusing, which results in low-cost and eases rapid production with automatic PM assembly [15]–[17].

To improve the performance of spoke-type IPM machines, many studies have been documented. Several spoke-type IPM machines with different slot-pole combinations are compared in [17], which confirms that machines with higher pole numbers exhibit higher torque density. The work [18] employs modular spoke-type consequent-pole rotor that shows a slight increase of average torque and a clear reduction of torque ripple. A novel alternate air space barrier structure is proposed for spoke-type IPM machines in [19] for higher torque capability and better manufacturability. For torque ripple reduction, a sinusoidally axial skewing PM configuration is proposed in [20]. The work [21] proposes a high power density IPM machine employing 12-slot/10-pole combination, spoke-type PMs, and modular rotor laminations.

Recently, asymmetric IPM (AIPM) rotor topologies become attractive for torque characteristic improvement in literature. The work [22] proposes a hybrid-layer IPM rotor topology that shows significant torque enhancement due to utilizing magnetic field shifting (MFS) effect and significant torque ripple reduction, simultaneously. In [23], asymmetric V-shape PMs combined with outer flux barrier designs are employed in a novel AIPM machine, which can achieve significant torque enhancement compared with the conventional V-shape IPM machine in Toyota Prius 2010 with the same PM usage. The work [24] proposes an inset IPM design that achieves the MFS effect using asymmetric location of PMs, which shows clear increase of torque. Additional flux barrier near the rotor surface is used in V-shape [25] and Bar-shape [26] IPM machines to improve the torque performance. In [27], a novel asymmetric IPM (AIPM) topology with symmetrical flux barrier and asymmetric PMs is proposed that shows clear torque enhancement

but also exhibits quite complex structure. Except for torque enhancement, asymmetric rotor topologies are also employed in IPM machines as effective methods for torque ripple reduction [28], [29]. In [30], a spoke-type IPM machine with asymmetric profile is proposed for torque ripple reduction and vibration suppression. Spoke-type IPM topologies with assisted poles that exhibit asymmetry between adjacent pole geometries are proposed in [31] and [32] for torque pulsating reduction. It shows significant suppression of torque ripple but also results in the decrease of average torque.

The work [33] has proposed a novel AIPM rotor topology with spoke-type PMs and asymmetric flux barrier structure, which shows torque enhancement due to MFS effect for a 24-slot/4-pole IPM synchronous machine with single-layer overlapping windings, compared with a conventional spoke-type IPM machine and a spoke-type IPM machine with symmetrical flux barrier design using the same stator, rotor diameter, and PM dimensions. This article extends the paper [33] and further investigates utilization of the proposed spoke-type AIPM rotor topology in IPM machine with nonoverlapping windings by employing the proposed topology in 12-slot/8-pole IPM machines. By comparing with a conventional spoke-type IPM topology and an existing spoke-type AIPM design using asymmetric rotor profile [30], all with the same stator, rotor diameter, and PM dimensions, this article confirms that significant torque enhancement, torque ripple reduction, and cogging torque suppression can be achieved simultaneously using the proposed spoke-type AIPM topology without introducing any extra cost in 12-slot/8-pole IPM machines with nonoverlapping windings. Besides, the measured results of the AIPM prototype are provided and compared with finite element (FE) predicted results for verification.

This article is organized as follows. Section II describes rotor topologies of the proposed AIPM-I, existing AIPM-II, and conventional IPM machines, all with spoke-type PMs, and the shared 12-slot/8-pole stator equipped with single-layer nonoverlapping windings and design optimization of machines with the same stator, rotor diameter, and PM dimensions. The influence of asymmetric flux barrier dimensions on the proposed AIPM machine is investigated in Section III with particular emphasis on torque characteristics including average torque, torque ripple, and cogging torque at open-circuit condition. The performances of final optimal designs of three machines, including open-circuit and torque characteristics, constant power speed range (CPSR), efficiency, loss, and mechanical stress, are compared in Section IV to confirm the merits of the proposed AIPM topology. Sections V and VI provide the experimental results and conclusion, respectively.

II. MACHINE TOPOLOGY AND DESIGN OPTIMIZATION

A. Proposed Machine Topology

Fig. 1(a)–(c) shows rotor cross sections of the proposed AIPM-I machine with asymmetric flux barriers, an existing AIPM-II machine employing asymmetric rotor profile [30], and a conventional IPM machine, respectively, all using spoke-type PM configuration. As shown in Fig. 1(a), the asymmetric flux barrier of the AIPM-I machine is located between rotor surface

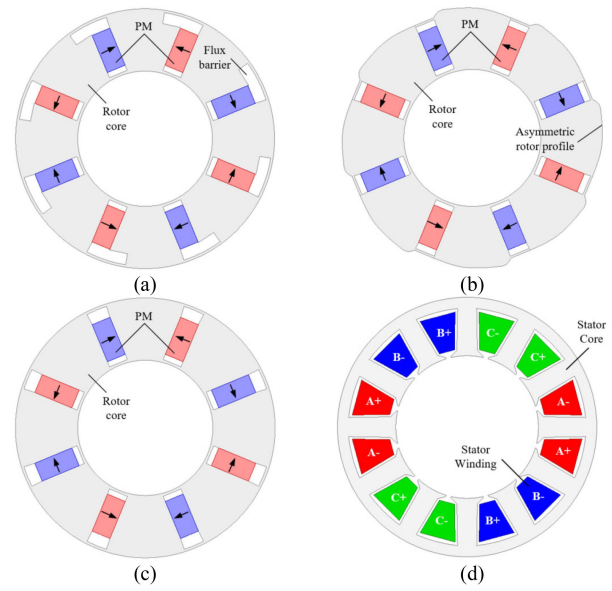


Fig. 1. Spoke-type IPM machine topologies. (a) Proposed AIPM-I topology with asymmetric flux barriers. (b) Existing AIPM-II topology with asymmetric rotor profile [30]. (c) Conventional IPM topology. (d) Shared 12-slot/8-pole stator design.

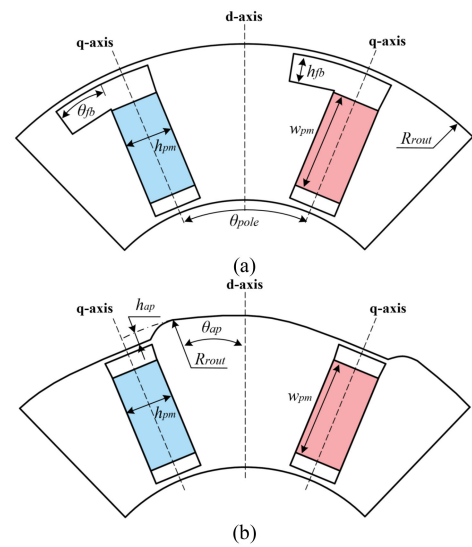


Fig. 2. Rotor schematic and some key geometric design parameters. (a) AIPM-I. (b) AIPM-II.

and PM cavity at the left side of PM in each pole. In the AIPM-II machine, the asymmetric rotor profile results in unequal air-gap length and the minimum air-gap length is the same as the uniform air-gap length in AIPM-I and IPM machines. Arrows in PMs denote magnetization directions. Moreover, the same 12-slot/8-pole stator with three-phase single-layer nonoverlapping windings is shared by three machines and the winding configuration is shown in Fig. 1(d).

Fig. 2(a) and (b) illustrates the key geometric parameters of rotor structures of both the proposed AIPM-I and the existing AIPM-II machine topologies, respectively. R_{out} is the outer diameters of the rotor core and θ_{pole} is the pole arc of one pole. Besides, w_{pm} and h_{pm} are the width and height of the spoke-type

PM, respectively. For the AIPM-I machine, θ_{fb} and h_{fb} are the width and height of the asymmetric flux barrier, respectively. To normalize the flux barrier features, the width and height factors α_w and α_h are defined as

$$\alpha_w = \frac{\theta_{fb}}{\theta_{pole}} \quad (1)$$

$$\alpha_h = \frac{h_{fb}}{\delta} \quad (2)$$

where δ is the air-gap length.

As shown in Fig. 2(b), a nonuniform rotor profile with asymmetric distribution is employed, which results in unequal air-gap length. The maximum air-gap length exists near the outer iron bridge in which the additional air-gap length compared with the minimum air-gap length δ is h_{ap} . The position of minimum air-gap length, in which the air-gap length is the same as δ in AIPM-I and IPM machines with uniform air-gap, is described by arc pitch θ_{ap} . For normalization, the asymmetric profile position and maximum air-gap length factors β_{ap} and β_{agl} are defined as

$$\beta_{ap} = \frac{2\theta_{ap}}{\theta_{pole}} \quad (3)$$

$$\beta_{agl} = \frac{h_{ap}}{\delta}. \quad (4)$$

B. Multiobjective Optimization

To obtain optimal designs of both the proposed AIPM-I and existing AIPM-II machines with asymmetric features, multiobjective design optimization [34] is carried out based on genetic algorithm (GA) and two-dimensional time-stepping FE analysis.

The general optimization objectives for both AIPM machines include the following:

- 1) maximizing average torque using the maximum torque per ampere (MTPA) method;
- 2) minimizing torque ripple ratio T_{ripple} at the maximum torque condition.

The torque ripple ratio is defined as

$$T_{\text{ripple}} = \frac{T_{\text{p-p}}}{T_{\text{syn}}} \times 100\% \quad (5)$$

where T_{syn} and $T_{\text{p-p}}$ are the average torque and the peak-to-peak value of torque waveform, respectively.

For a fair comparison, both AIPM-I and AIPM-II machines use the fixed stator design, rotor outer and inner radii, axial length, and spoke-type PM dimensions that are the same as the conventional spoke-type IPM benchmark. The same materials of rotor laminations and PMs are also used for all three machines. Besides, fixed 10 A(peak)/7.07 A(rms) current and 750 r/min rotation speed are applied in the design optimization. To ease the optimization process, the range of geometric variables that are normalized factors defined in (1)–(4) are limited as listed in Table I.

The optimization results and selected final optimal designs of AIPM-I and AIPM-II machines are shown in Fig. 3(a) and (b), respectively. By using the multiobjective optimization, the final

TABLE I
RANGE OF GEOMETRIC VARIABLES

| Variable | Range | Variable | Range |
|------------|----------|---------------|-----------|
| α_w | [0, 0.6] | β_{ap} | [0, 0.77] |
| α_h | [0, 8] | β_{agl} | [0, 8] |

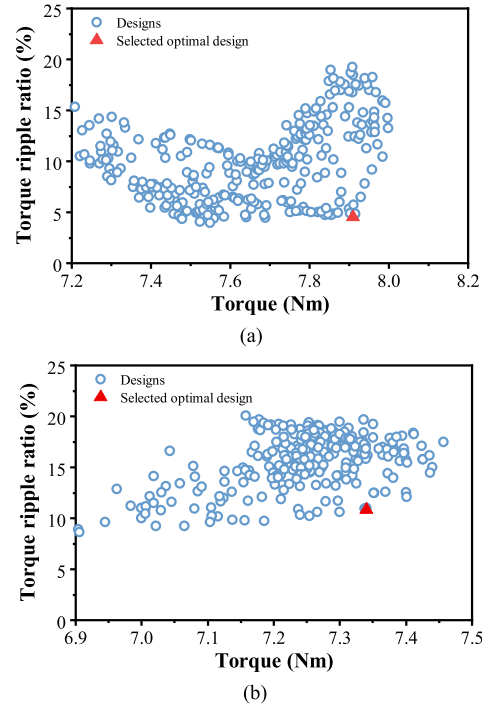


Fig. 3. Optimization results. (a) AIPM-I. (b) AIPM-II.

optimal designs of three machines are obtained and some main design parameters are shown in Table II.

III. EFFECT OF ASYMMETRIC FLUX BARRIER DIMENSIONS IN THE PROPOSED AIPM-I MACHINE

Although the final optimal design of the proposed AIPM-I machine is obtained in Section II, it is essential to investigate the effect of asymmetric flux barrier dimensions that are the main features of the AIPM-I topology based on FE analysis, with particular emphasis on torque characteristics, i.e., average torque, torque ripple, and cogging torque at open-circuit condition. The average torque and torque ripple are calculated at fixed 10-A peak current, 750 r/min, and MTPA. In this section, the parameters of the AIPM-I machine are fixed as shown in Table II except for sweeping parameters and the results of the final optimal design are highlighted.

A. Flux Barrier Width

The influences of asymmetric flux barrier width, denoted by the width factor α_w , on average torque, torque ripple, and cogging torque are shown in Fig. 4, in which the cogging torque is the peak-to-peak value of the cogging torque waveform.

TABLE II
MAIN DESIGN PARAMETERS OF TOPOLOGIES

| Parameters | Unit | AIPM-I | AIPM-II | IPM |
|--|-----------------|---------------------------------------|---------|-----|
| No. of stator slots, N_s | - | | 12 | |
| No. of pole pairs, p | - | | 4 | |
| Phase number, N_p | - | | 3 | |
| Stator winding type | - | Single-layer non-overlapping windings | | |
| Stator outer radius | mm | | 50 | |
| Axial length, L_t | mm | | 50 | |
| Stator tooth width, w_s | mm | | 7.9 | |
| Stator slot height, h_s | mm | | 18.2 | |
| Stator slot opening, w_{so} | mm | | 2 | |
| Turn number per phase, N_{ph} | - | | 480 | |
| Air-gap length, δ | mm | | 0.6 | |
| R_{rin} | mm | | 14 | |
| R_{rou} | mm | | 26.9 | |
| Total PM volume, V_{mag} | mm ³ | | 13280 | |
| PM material and grade | - | Nd-Fe-B, N38 | | |
| Remanence of PM, B_r | T | | 1.235 | |
| Relative permeability of PM, μ_r | - | | 1.05 | |
| Outer iron bridge thickness, b_{out} | mm | | 0.5 | |
| Inner iron bridge thickness, b_{in} | mm | | 0.5 | |
| w_{pm} | mm | | 8.3 | |
| h_{pm} | mm | | 4 | |
| α_w | - | 0.16 | - | - |
| α_h | - | 4.83 | - | - |
| β_{ap} | - | - | 0.58 | - |
| β_{agl} | - | - | 2.08 | - |

As can be seen, the optimal designs for maximum average torque and minimum torque ripple and cogging torque all exist for α_w . The increase of flux barrier width can generally increase the maximum torque significantly except for large α_w . Optimal α_w for minimum torque ripple and cogging torque are similar, but there is a notable difference between α_w for maximum torque and minimum torque ripple, as the optimum values for average torque, torque ripple, and cogging torque are around 0.28, 0.11, and 0.14, respectively. The compromise has been made for the final optimal design of the AIPM-I machine as α_w is not the optimum value of any torque characteristic, but all three torque characteristics are desirable. Besides, it also shows that each specific torque performance can be further improved, albeit with the sacrifice of other torque characteristics.

B. Flux Barrier Height

Fig. 5 shows the effect of flux barrier height, denoted by height factor α_h , on torque characteristics in the AIPM-I machine. Similar to α_w , flux barrier height also shows significant influence on torque characteristics of the AIPM-I machine, and optimal values exist for all performances. In detail, the selected flux barrier height factor of final optimal design, 4.83, can approximately reach the minimum torque ripple. The highest maximum torque may be obtained by using relatively larger α_h but also resulting in the increase of both torque ripple and cogging torque.

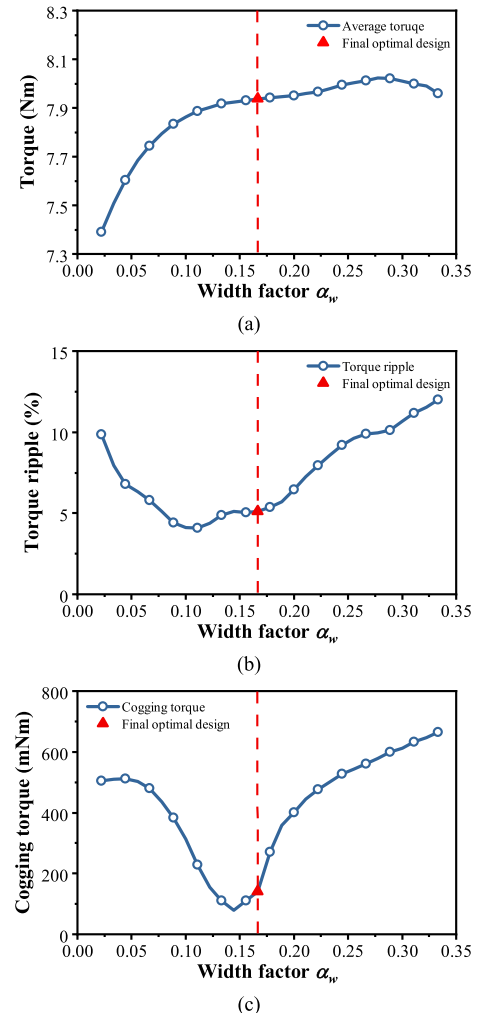


Fig. 4. Influence of flux barrier width factor α_w . (a) Average torque. (b) Torque ripple. (c) Cogging torque.

Moreover, although cogging torque of the final optimal machine design is not at a high level, it can be further reduced, albeit with the sacrifice of both average torque and torque ripple at 10-A current.

IV. ELECTROMAGNETIC PERFORMANCE COMPARISON

In this section, electromagnetic performance of the final optimal design of the proposed AIPM-I machine is compared with those of the existing AIPM-II and the conventional IPM machines to reveal the merits and demerits of the proposed spoke-type AIPM topology. The cross sections of final optimal designs of three machines are shown in Fig. 6, together with their open-circuit flux density and flux line distributions.

A. Open-Circuit Characteristics

Fig. 7(a) and (b) compares the open-circuit flux density waveforms and spectra, respectively. The proposed AIPM-I machine shows clear asymmetric distribution of flux density, while the AIPM-II machine has notably distorted waveform, compared with the conventional IPM machine. The fundamental

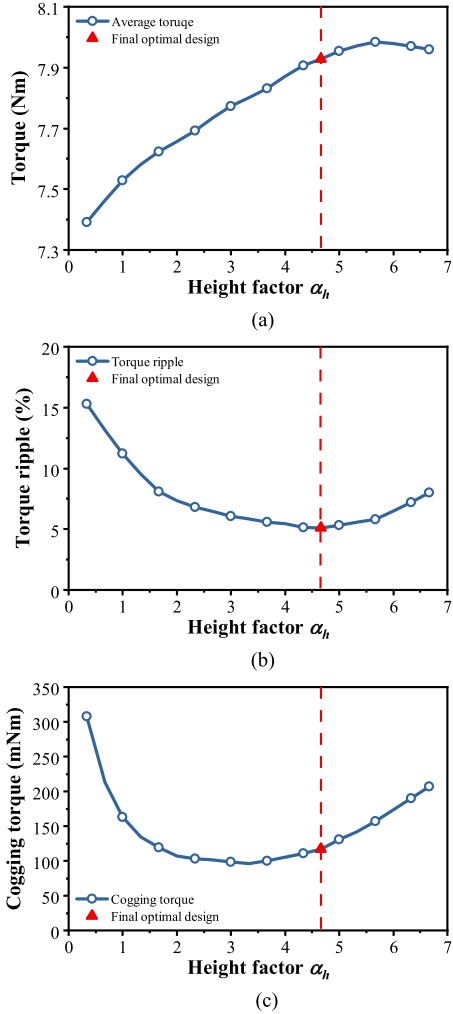


Fig. 5. Influence of flux barrier height factor α_h . (a) Average torque. (b) Torque ripple. (c) Cogging torque.

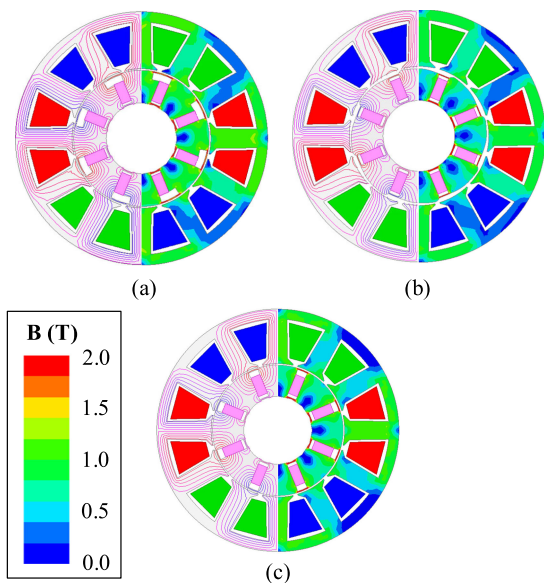


Fig. 6. Cross sections and distributions of open-circuit flux density and flux line of three final optimal machines. (a) AIPM-I. (b) AIPM-II. (c) IPM.

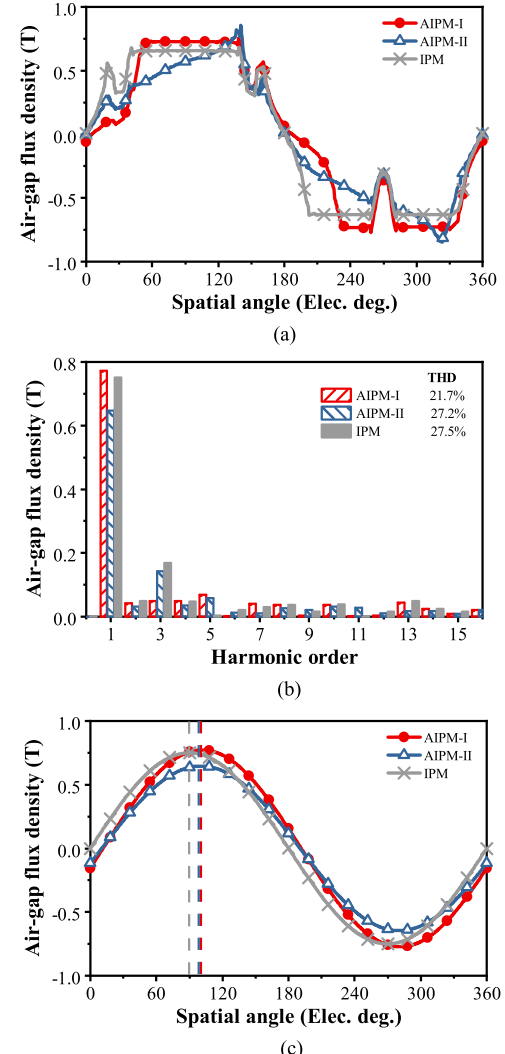
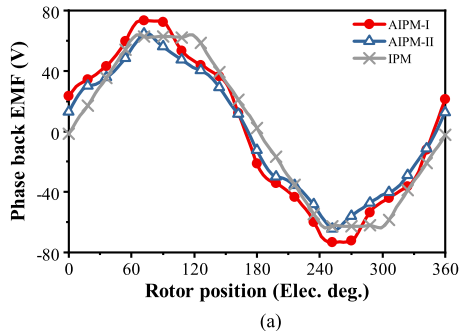


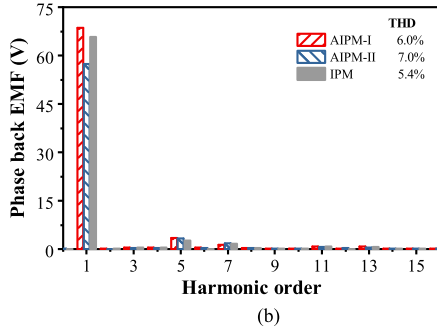
Fig. 7. Open-circuit air-gap flux densities. (a) Waveforms. (b) Spectra. (c) Fundamental components.

amplitude of the AIPM-I machine is slightly higher than that of the IPM machine, but the AIPM-II machine shows significantly smaller fundamental amplitude mainly due to the asymmetric rotor profile that clearly increases the equivalent air-gap length. Besides, the AIPM-I machine shows the smallest total harmonic distortion (THD) compared with both AIPM-II and IPM machines as the amplitude of the third-order harmonic component in the AIPM-I machine is particularly smaller than those of other machines. The fundamental components of air-gap flux densities in three machines are compared in Fig. 7(c) with emphasis on phases of waveforms, which shows that asymmetric structures in AIPM-I and AIPM-II machines result in the phase shifting of fundamental components.

Fig. 8 shows the waveforms and spectra of open-circuit back electromotive force (EMF) in three machines. As can be seen, waveforms of AIPM-I and AIPM-II machines have clear distortion, compared with that of IPM machine. The AIPM-I machine has the highest fundamental amplitude of back EMF,

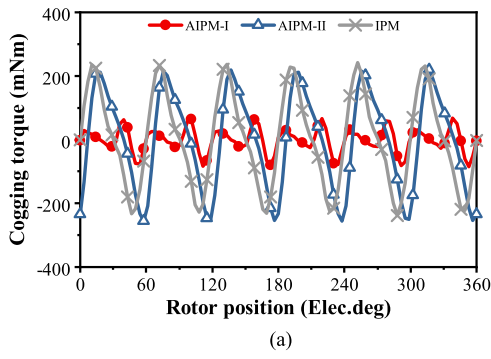


(a)

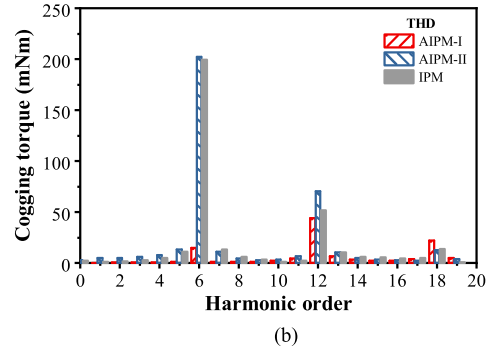


(b)

Fig. 8. Open-circuit back EMFs of Phase A windings at 750 r/min. (a) Waveforms. (b) Spectra.



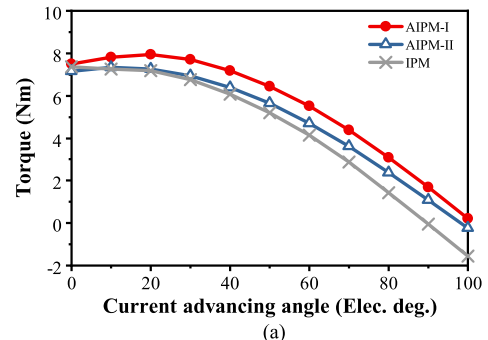
(a)



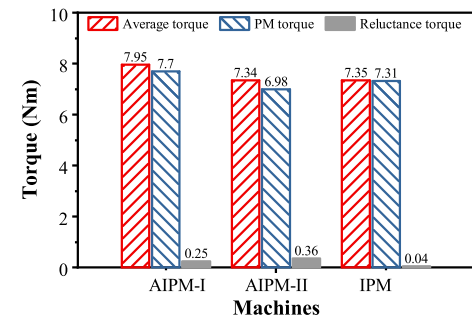
(b)

Fig. 9. Cogging torques. (a) Waveforms. (b) Spectra.

followed by that of IPM machine with slightly smaller value, and the fundamental amplitude of the AIPM-II machine is notably smaller than those of the other machines, corresponding to its smallest fundamental open-circuit flux density. Moreover, all three machines have similar THDs of back EMFs.



(a)



(b)

Fig. 10. Average torques at 750 r/min and 10 A. (a) Average torque. (b) Torque components at maximum torque conditions.

Fig. 9 compares cogging torques of three machines at open-circuit condition, including the waveforms [Fig. 9(a)] and spectra [Fig. 9(b)], which confirms the significant reduction of cogging torque in the AIPM-I machine due to the elimination of sixth-order torque harmonic, as the peak-to-peak value of the AIPM-I machine is about 75% smaller than those of both AIPM-II and IPM machines.

B. Average Torque

Fig. 10(a) compares the torque-current angle performance of three machines at 10 A and 750 r/min. It shows significant increase of average torque in the AIPM-I machine, compared with the AIPM-II and IPM machines. More specifically, around 8% torque increase can be achieved in the AIPM-I machine, compared with both AIPM-II and IPM machines, as AIPM-II and IPM machines have similar maximum torque, 7.34 and 7.35 Nm, at 10 A, 750 r/min, and MTPA. Besides, it is also found that both AIPM-I and AIPM-II machines reach their maximum torque at around 20 and 16 elec. degs., which are clearly larger than that of IPM machine at about 3 elec. degs. It can be regarded as a result of the phase-shifting in fundamental components waveforms of open-circuit flux density in both AIPM machines.

The torque components in all three machines at their maximum torque conditions are extracted into two components: PM torque and reluctance torque by using frozen permeability method [35] as shown in Fig. 10(b). In general, the reluctance torque components are notably smaller than PM torque components in all three machines, respectively, due to using nonoverlapping windings. It is also found that the torque enhancement of the AIPM-I machine is achieved because of both higher PM and

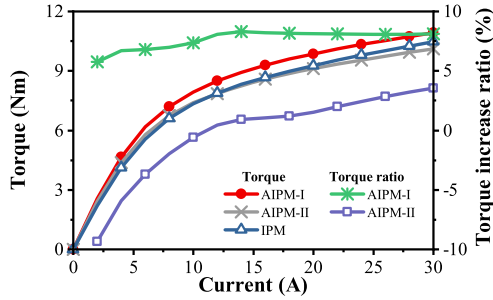


Fig. 11. Maximum torque versus current with MTPA.

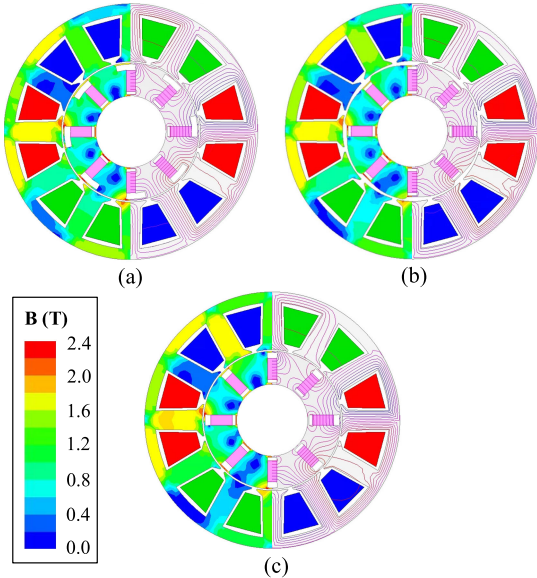


Fig. 12. Comparison of flux density and flux line distributions at 10 A, 750 r/min, and MTPA. (a) AIPM-I. (b) AIPM-II. (c) IPM.

reluctance torque compared with the IPM machine. Moreover, although the AIPM-II machine has the smallest PM torque, corresponding to its smallest fundamental component of both open-circuit flux density and back EMF, it can reach similar maximum average torque because of the highest reluctance torque.

To investigate the effect of armature reaction on the maximum average torque of three machines, the maximum torques at different current are calculated and compared in Fig. 11. It reveals that the proposed AIPM-I machine remains around 7%–9% torque enhancement compared with the IPM machine across the whole current range, while the AIPM-II machine has higher maximum torque than the IPM machine at high load condition, but the torque enhancement diminishes at low load condition. Moreover, the distributions of magnetic flux density and flux line in three machines at 10 A, 750 r/min, and MTPA are compared in Fig. 12.

The average torque-current angle characteristics of three machines considering both rotation directions and operation modes at 10 A and 750 r/min are compared in Fig. 13. At anticlockwise rotation direction of rotor, the phase sequence of stator windings in three machines is shown in Fig. 1(d), while at clockwise rotor rotation direction, the phase sequence is correspondingly

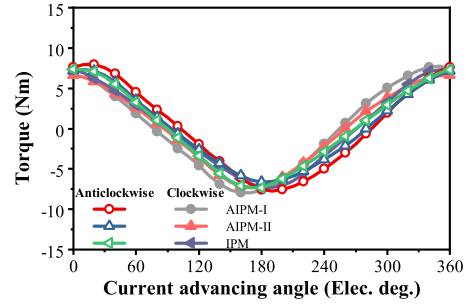


Fig. 13. Comparison of torque-current angle characteristics at 10 A, 750 r/min, and different rotation directions.

TABLE III
COMPARISON OF MAXIMUM TORQUES (UNIT: Nm)

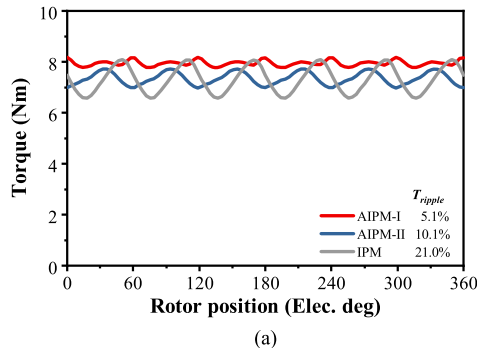
| Machines | Anticlockwise direction | | Clockwise direction | |
|----------|-------------------------|----------------|---------------------|----------------|
| | Motor mode | Generator mode | Motor mode | Generator mode |
| AIPM-I | 7.95 | 7.72 | 7.72 | 7.95 |
| AIPM-II | 7.34 | 6.60 | 6.60 | 7.34 |
| IPM | 7.35 | 7.35 | 7.35 | 7.35 |

changed by swapping the B-phase and C-phase windings. As can be seen, the rotation directions show clear effect on torque-angle characteristics and maximum torque in both AIPM machines. Compared with the anticlockwise direction, AIPM machines at the clockwise direction show smaller maximum torque at the motor mode but higher maximum torque at the generator mode, while the maximum torque of the IPM machine benchmark at both motor and generator modes and rotation directions remains the same, as shown in Table III. Therefore, at the motor mode, both AIPM machines have smaller maximum torque at clockwise direction than at anticlockwise direction, although AIPM machines at generator modes also shows higher torque at clockwise direction than those at the anticlockwise direction. Besides, it is also found that the proposed AIPM-I machine has the highest torque at both motor and generator modes and rotation directions, compared with AIPM-II and IPM machines.

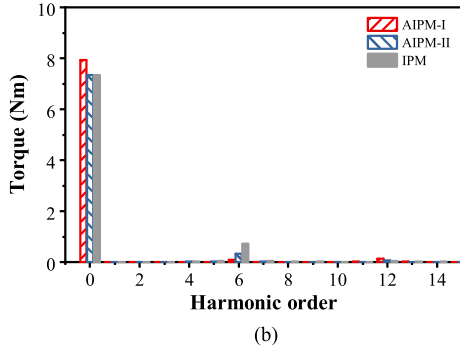
C. Torque Ripple

The torque waveforms in three machines at 10 A and 750 r/min and MTPA are compared in Fig. 14(a). As can be seen, the proposed AIPM-I machine shows the smallest torque ripple, 5.1%, followed by the AIPM-II machine, 10.1%, compared with the conventional spoke-type IPM machine, 21.0%, which achieves around 75.7% and 51.9% of torque ripple reduction, respectively. The spectra of torque waveforms of three machines are shown in Fig. 14(b), which shows that the torque ripple reduction at 10 A, 750 r/min, and MTPA in both AIPM-I and AIPM-II machines are mainly due to the suppression of the sixth-order torque component.

To confirm the torque ripple reduction in AIPM machines across the current range, the torque ripple ratio T_{ripple} of three machines at maximum torque condition of different current amplitudes are compared in Fig. 15. It shows that the feature of low torque ripple characteristic in the AIPM-I machine remains across the whole current range as it has the smallest torque ripple



(a)



(b)

Fig. 14. Comparison of torque ripples at 10 A and 750 r/min. (a) Waveforms. (b) Spectra.

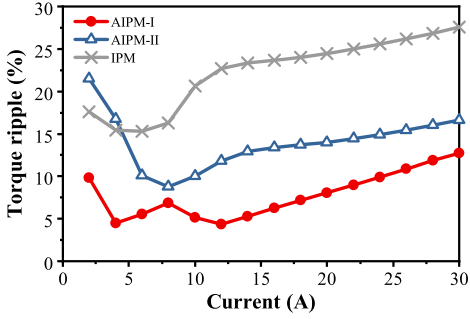


Fig. 15. Torque ripples versus current with MTPA.

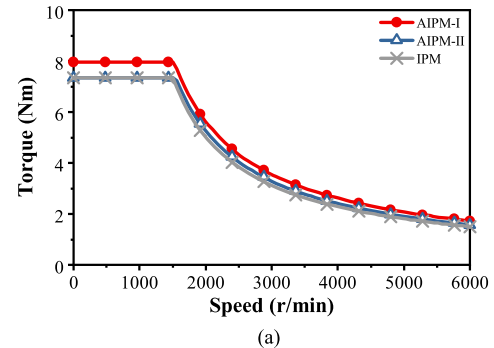
and T_{ripple} is generally smaller than 10%. Moreover, the existing AIPM-II machine also shows smaller torque ripple compared with the IPM machine except for at low current conditions.

D. CPSR, Efficiency, and Losses

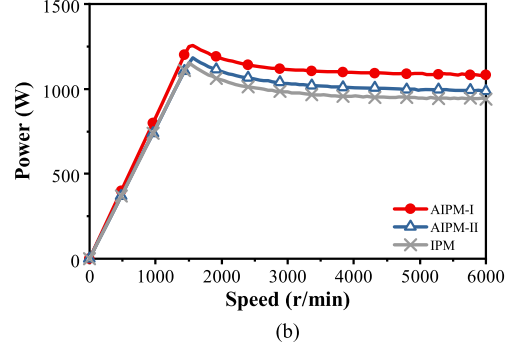
The CPSR performances in three machines at the maximum current 10 A, maximum dc voltage 200 V, and MTPA are compared in Fig. 16. As can be seen, the proposed AIPM-I machine remains the highest torque and power across the whole speed range compared with the existing AIPM-II and the conventional IPM machines.

The variations of efficiency, iron loss, and PM eddy-current loss across the speed range in three machines under the same 20-W copper loss are compared in Fig. 17 and Table IV.

In general, the efficiencies of three machines increase gradually with the increase of speed and the proposed AIPM-I machine has the highest efficiency due to torque enhancement across the investigated speed range. The conventional IPM machine shows



(a)



(b)

Fig. 16. Comparison of CPSR performance at maximum 10-A current, maximum 200-V dc voltage, and MTPA. (a) Torque-speed curve. (b) Power-speed curve.

TABLE IV
COMPARISON OF EFFICIENCY AND LOSS CHARACTERISTICS

| Performance | AIPM-I | AIPM-II | IPM |
|--------------------------|--------|---------|------|
| Speed (r/min) | 3000 | 3000 | 3000 |
| Torque (Nm) | 2.62 | 2.21 | 2.41 |
| Efficiency (%) | 94.6 | 93.8 | 93.7 |
| Copper loss (W) | 20 | 20 | 20 |
| Iron loss (W) | 13.7 | 11.7 | 15.3 |
| PM eddy-current loss (W) | 0.35 | 0.33 | 0.34 |

the highest iron loss compared with other AIPM machines, while the existing AIPM-II machine has the smallest iron loss. The difference of iron losses between topologies becomes significant at a high speed. Besides, the PM eddy-current losses of three machines are similar across the speed range.

E. Mechanical Analysis

To compare the rotor mechanical strength of three machines at high speed, the von-Mises stress distributions of three machines at 6000 r/min are compared in Fig. 18. As can be seen, the maximum stress regions of three machines are all located near the inner iron bridges and the maximum stresses are generally similar, which confirms the similar mechanical strength of three machine topologies.

V. EXPERIMENTAL VALIDATION

To validate the proposed design concept and FE-predicted results, the final optimal design of the AIPM-I machine has been fabricated and the prototype has been measured based on the design parameters in Table I. The rotor and stator of the AIPM-I

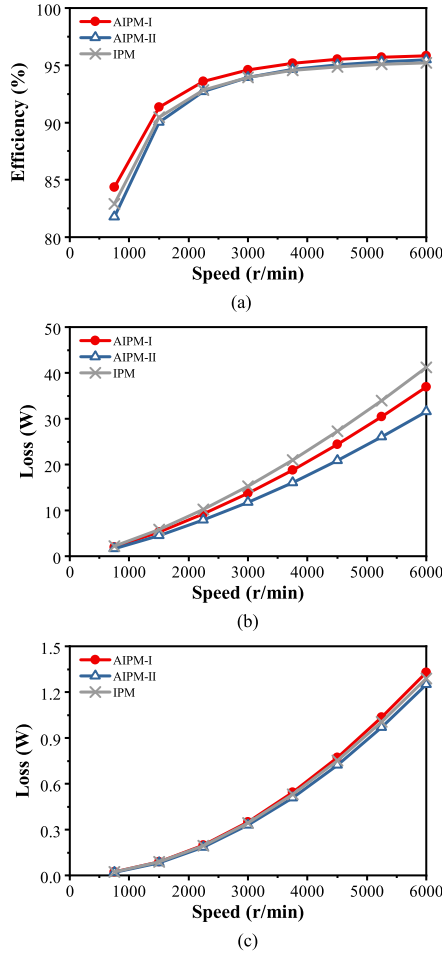


Fig. 17. Comparison of efficiency, iron loss, PM eddy-current loss under 20-W copper loss, and MTPA. (a) Efficiency. (b) Iron loss. (c) PM eddy-current loss.

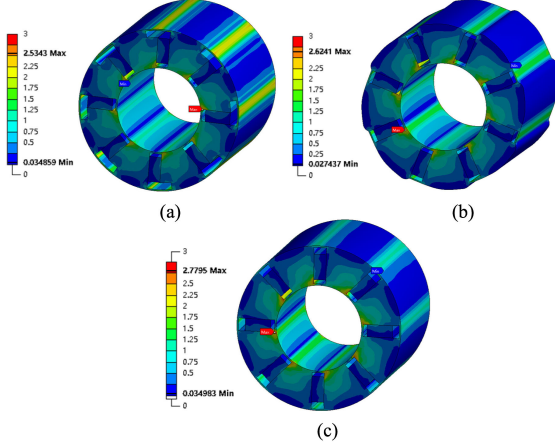


Fig. 18. Comparison of von-Mises stress distributions at 6000 r/min. (a) AIPM-I. (b) AIPM-II. (c) IPM.

machine prototype are shown in Fig. 19(a) and (b), respectively, while the test bench is demonstrated in Fig. 19(c).

The measured line back EMF at 750 r/min is compared with FE-predicted results in Fig. 20. The measured results match well with the FE-predicted results, as the measured fundamental

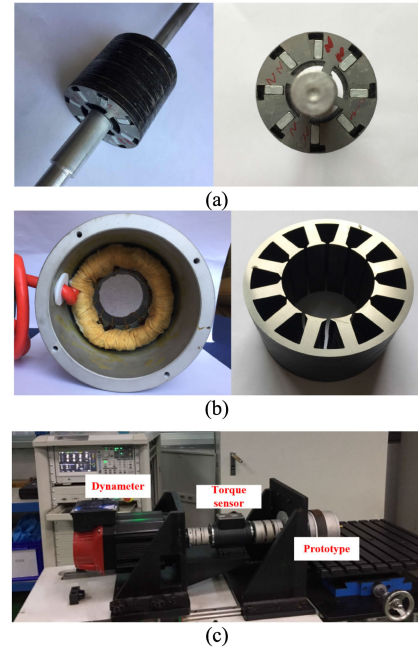


Fig. 19. Photos of AIPM-I machine prototype and test bench. (a) Rotor. (b) Stator and lamination. (c) Test bench.

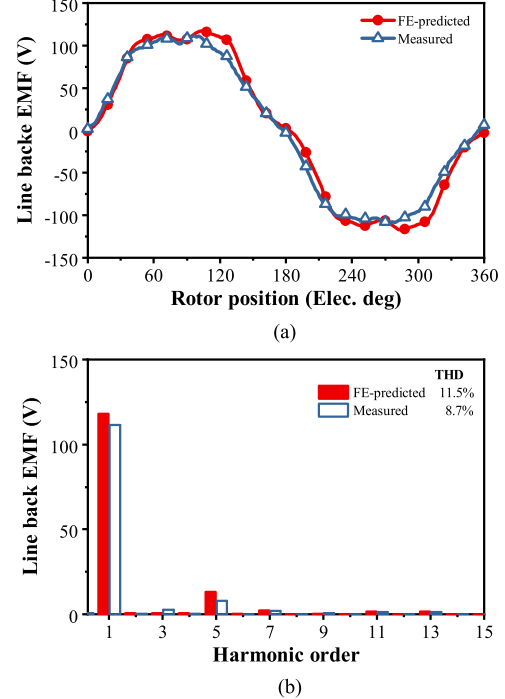


Fig. 20. Line back EMFs at 750 r/min. (a) Waveforms. (b) Spectra.

amplitude is only around 5.6% smaller than that of FE-predicted result. Besides, the measured cogging torque waveform is compared with that of FE-predicted result at open-circuit condition as shown in Fig. 21.

To measure the static torque of the prototype, dc current I_p is injected into three-phase windings with the current configuration $I_A = I_p$, $I_B = -I_p/2$, and $I_C = -I_p/2$. The dc current in stator

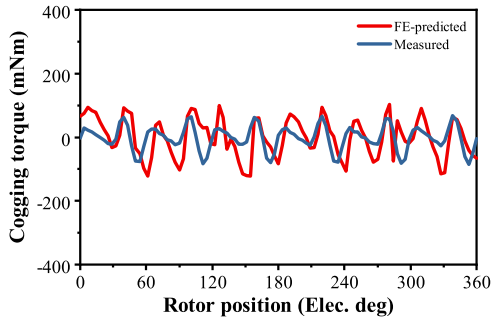


Fig. 21. Comparison of cogging torque waveforms.

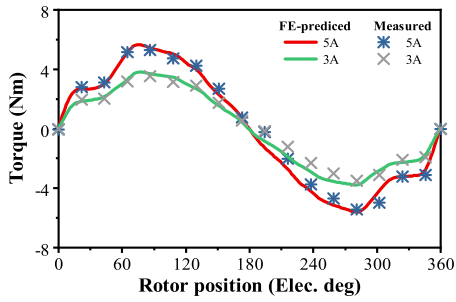


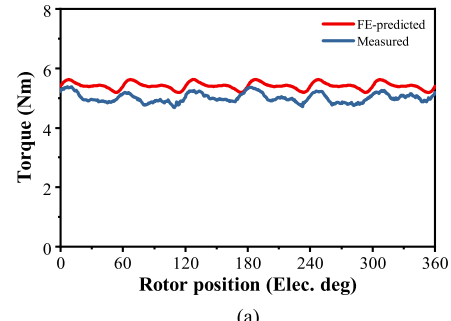
Fig. 22. Static torques at different currents.

windings remains constant during the experiment while the relative position between stator and rotor is changed gradually and the static torque is measured by a torque sensor. The measured static torque of the AIPM-I machine prototype at two different I_p conditions: 5 A and 3 A are compared with FE-predicted results in Fig. 22, which also shows good agreement. The measured current conditions are selected due to the restriction of test bench.

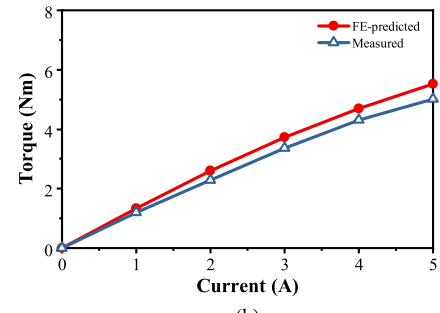
The torque waveform of the prototype is measured by dynamic experiments at 5 A and 750 r/min using MTPA and is compared with FE-predicted torque waveform at the same condition in Fig. 23(a). By performing dynamic experiments, the measured maximum average torques at different currents are compared with the FE-predicted results in Fig. 23(b).

VI. CONCLUSION

This article proposes a novel spoke-type AIPM machine topology featured by asymmetric flux barrier for IPM synchronous machines with 12-slot/8-pole nonoverlapping windings. It can achieve significant torque enhancement and torque ripple reduction compared with both the existing spoke-type AIPM machine with asymmetric rotor profile and the conventional spoke-type IPM machine using the same stator, rotor diameter, and PM dimensions almost without introducing any extra cost. The parametric study of asymmetric flux barrier dimensions by using FE analysis reveals that both flux barrier width and height show clear effect on torque characteristics in the proposed AIPM-I machine. The comparison of electromagnetic performance confirms both the torque enhancement and torque ripple reduction of the proposed AIPM-I machine across the wide current range, while it also reveals the notable cogging



(a)



(b)

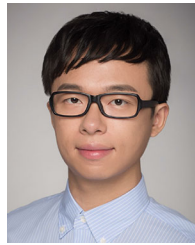
Fig. 23. Comparison between dynamic torque results. (a) Torque waveforms at 5 A and 750 r/min. (b) Maximum average torque versus current.

torque reduction simultaneously. Finally, experimental results of the AIPM-I machine prototype are provided for verification.

REFERENCES

- [1] Z. Zhu and D. Howe, "Electrical machines and drives for electric, hybrid, and fuel cell vehicles," *Proc. IEEE*, vol. 95, no. 4, pp. 746–765, Apr. 2007.
- [2] A. S. Thomas, Z. Q. Zhu, and G. W. Jewell, "Comparison of flux switching and surface mounted permanent magnet generators for high-speed applications," *IET Electr. Syst. Transp.*, vol. 1, no. 3, pp. 111–116, Sep. 2011.
- [3] I. Boldea, L. N. Tutelea, L. Parsa, and D. Dorrell, "Automotive electric propulsion systems with reduced or no permanent magnets: An overview," *IEEE Trans. Ind. Electron.*, vol. 61, no. 10, pp. 5696–5711, Jan. 2014.
- [4] Z. Zhu, W. Chu, and Y. Guan, "Quantitative comparison of electromagnetic performance of electrical machines for HEVs/EVs," *CES Trans. Electr. Mach. Syst.*, vol. 1, no. 1, pp. 37–47, Jul. 2017.
- [5] Z. S. Du and T. A. Lipo, "Efficient utilization of rare earth permanent-magnet materials and torque ripple reduction in interior permanent-magnet machines," *IEEE Trans. Ind. Appl.*, vol. 53, no. 4, pp. 3485–3495, Jul./Aug. 2017.
- [6] P. B. Reddy, A. M. El-Refaie, K. Huh, J. K. Tangudu, and T. M. Jahns, "Comparison of interior and surface PM machines equipped with fractional-slot concentrated windings for hybrid traction applications," *IEEE Trans. Energy Convers.*, vol. 27, no. 3, pp. 593–602, Sep. 2012.
- [7] X. Liu, H. Chen, J. Zhao, and A. Belahcen, "Research on the performances and parameters of interior PMSM used for electric vehicles," *IEEE Trans. Ind. Electron.*, vol. 63, no. 6, pp. 3533–3545, Jun. 2016.
- [8] K. Kamiev, J. Montonen, M. P. Ragavendra, J. Pyrhönen, J. A. Tapia, and M. Niemelä, "Design principles of permanent magnet synchronous machines for parallel hybrid or traction applications," *IEEE Trans. Ind. Electron.*, vol. 60, no. 11, pp. 4881–4890, Nov. 2013.
- [9] S. Zhu, W. Chen, M. Xie, C. Liu, and K. Wang, "Electromagnetic performance comparison of multi-layered interior permanent magnet machines for EV traction applications," *IEEE Trans. Magn.*, vol. 54, no. 11, pp. 1–5, Nov. 2018.
- [10] F. Momen, K. Rahman, and Y. Son, "Electrical propulsion system design of Chevrolet bolt battery electric vehicle," *IEEE Trans. Ind. Appl.*, vol. 55, no. 1, pp. 376–384, Jan./Feb. 2019.
- [11] Y. Hu, S. Zhu, C. Liu, and K. Wang, "Electromagnetic performance analysis of interior PM machines for electric vehicle applications," *IEEE Trans. Energy Convers.*, vol. 33, no. 1, pp. 199–208, Jul. 2018.

- [12] X. Chen, J. Wang, V. I. Patel, and P. Lazari, "A nine-phase 18-slot 14-pole interior permanent magnet machine with low space harmonics for electric vehicle applications," *IEEE Trans. Energy Convers.*, vol. 31, no. 3, pp. 860–871, Mar. 2016.
- [13] Y. Honda, T. Higaki, S. Morimoto, and Y. Takeda, "Rotor design optimisation of a multi-layer interior permanent-magnet synchronous motor," in *Proc. IEE Proc. – Electr. Power Appl.*, Mar. 1998, vol. 145, no. 2, pp. 119–124.
- [14] S. S. Maroufian and P. Pillay, "Design and analysis of a novel PM-assisted synchronous reluctance machine topology with alnico magnets," *IEEE Trans. Ind. Appl.*, vol. 55, no. 5, pp. 4733–4742, Sep./Oct. 2019.
- [15] A. Fatemi, D. M. Ionel, M. Popescu, Y. C. Chong, and N. A. O. Demerdash, "Design optimization of a high torque density spoke-type PM motor for a formula e race drive cycle," *IEEE Trans. Ind. Appl.*, vol. 54, no. 5, pp. 4343–4354, Sep./Oct. 2018.
- [16] M. Si, X. Y. Yang, S. W. Zhao, and S. Gong, "Design and analysis of a novel spoke-type permanent magnet synchronous motor," *IET Electr. Power Appl.*, vol. 10, no. 6, pp. 571–580, Jul. 2016.
- [17] E. Carraro, N. Bianchi, S. Zhang, and M. Koch, "Design and performance comparison of fractional slot concentrated winding spoke type synchronous motors with different slot-pole combinations," *IEEE Trans. Ind. Appl.*, vol. 54, no. 3, pp. 2276–2284, May/Jun. 2018.
- [18] J. Li and K. Wang, "A novel spoke-type PM machine employing asymmetric modular consequent-pole rotor," *IEEE/ASME Trans. Mechatron.*, vol. 24, no. 5, pp. 2182–2192, Oct. 2019.
- [19] X. Ge, Z. Q. Zhu, J. B. Li, and J. T. Chen, "A spoke-type IPM machine with novel alternate airspace barriers and reduction of unipolar leakage flux by step-staggered rotor," *IEEE Trans. Ind. Appl.*, vol. 52, no. 6, pp. 4789–4797, Nov./Dec. 2016.
- [20] W. Zhao, T. A. Lipo, and B. Kwon, "Torque pulsation minimization in spoke-type interior permanent magnet motors with skewing and sinusoidal permanent magnet configurations," *IEEE Trans. Magn.*, vol. 51, no. 11, pp. 1–4, Nov. 2015.
- [21] A. M. EL-Refaie *et al.*, "Advanced high-power-density interior permanent magnet motor for traction applications," *IEEE Trans. Ind. Appl.*, vol. 50, no. 5, pp. 3235–3248, Sep./Oct. 2014.
- [22] Y. Xiao, Z. Q. Zhu, J. T. Chen, D. Wu, and L. M. Gong, "A novel asymmetric rotor interior PM machine with hybrid-layer PMs," in *Proc. IEEE Energy Convers. Congr. Expo.*, Detroit, MI, USA, 2020, pp. 2286–2291.
- [23] Y. Xiao *et al.*, "A novel asymmetric interior permanent magnet machine for electric vehicles," *IEEE Trans. Energy Convers.*, early access, Jan. 2021, doi: 10.1109/TEC.2021.3055260.
- [24] W. Zhao, T. A. Lipo, and B. Kwon, "Optimal design of a novel asymmetrical rotor structure to obtain torque and efficiency improvement in surface inset PM motors," *IEEE Trans. Magn.*, vol. 51, no. 3, pp. 1–4, Mar. 2015.
- [25] W. Zhao, F. Zhao, T. A. Lipo, and B.-I. Kwon, "Optimal design of a novel V-type interior permanent magnet motor with assisted barriers for the improvement of torque characteristics," *IEEE Trans. Magn.*, vol. 50, no. 11, pp. 1–4, Dec. 2014.
- [26] M. Ibrahim and P. Pillay, "Aligning the reluctance and magnet torque in permanent magnet synchronous motors for improved performance," in *Proc. IEEE Energy Convers. Congr. Expo.*, Portland, OR, Canada, 2018, pp. 2286–2291.
- [27] H. Yang, W. Wang, H. Lin, Z. Q. Zhu, S. Lyu, and S. Niu, "A novel hybrid-pole interior PM machine with magnet-axis-shifting effect," in *Proc. IEEE Int. Electr. Mach. Drives Conf.*, San Diego, CA, USA, 2019, pp. 273–279.
- [28] N. Bianchi, S. Bolognani, D. Bon, and M. Dai PrÉ, "Torque harmonic compensation in a synchronous reluctance motor," *IEEE Trans. Energy Convers.*, vol. 23, no. 2, pp. 466–473, Jun. 2008.
- [29] N. Bianchi, S. Bolognani, D. Bon, and M. Dai Pre, "Rotor flux-barrier design for torque ripple reduction in synchronous reluctance and PM-assisted synchronous reluctance motors," *IEEE Trans. Ind. Appl.*, vol. 45, no. 3, pp. 921–928, May/Jun. 2009.
- [30] Y. Jung, M. Park, and M. Lim, "Asymmetric rotor design of IPMSM for vibration reduction under certain load condition," *IEEE Trans. Energy Convers.*, vol. 35, no. 2, pp. 928–937, Jun. 2020.
- [31] Q. Chen, G. Xu, F. Zhai, and G. Liu, "A novel spoke-type PM motor with auxiliary salient poles for low torque pulsation," *IEEE Trans. Ind. Electron.*, vol. 67, no. 6, pp. 4762–4773, Jun. 2020.
- [32] Q. Chen, G. Xu, G. Liu, F. Zhai, and S. Eduku, "Reduction of torque ripple caused by slot harmonics in FSCW spoke-type FPM motors by assisted poles," *IEEE Trans. Ind. Electron.*, vol. 67, no. 11, pp. 9613–9622, Nov. 2020.
- [33] Y. Xiao, Z. Q. Zhu, J. T. Chen, D. Wu, and L. M. Gong, "A novel spoke-type asymmetric rotor interior PM machine," in *Proc. IEEE Energy Convers. Congr. Expo.*, Detroit, MI, USA, 2020, pp. 4050–4057.
- [34] Y. Li, D. Bobba, and B. Sarlioglu, "Design and optimization of a novel dual-rotor hybrid PM machine for traction application," *IEEE Trans. Ind. Electron.*, vol. 65, no. 2, pp. 1762–1771, Feb. 2018.
- [35] Z. Q. Zhu and W. Q. Chu, "Advanced frozen permeability technique and applications in developing high performance electrical machines," *Trans. China Electrotech. Soc.*, vol. 31, no. 20, pp. 13–29, Oct. 2016.



Yang Xiao received the B.Eng. and Ph.D. degrees in electrical engineering from the Huazhong University of Science and Technology, Wuhan, China, in 2013 and 2018, respectively. He is currently working toward the second Ph.D. degree in electronic and electrical engineering with The University of Sheffield, Sheffield, U.K.

His current research interests include the design of permanent magnet machines.



Z. Q. Zhu (Fellow, IEEE) received the B.Eng. and M.Sc. degrees from Zhejiang University, Hangzhou, China, in 1982 and 1984, respectively, and the Ph.D. degree from The University of Sheffield, Sheffield, U.K., in 1991, all in electrical and electronic engineering.

Since 1988, he has been with The University of Sheffield, where he is currently a Professor with the Department of Electronic and Electrical Engineering, the Head of the Electrical Machines and Drives Research Group, the Royal Academy of Engineering/Siemens Research Chair, the Academic Director of Sheffield Siemens Gamesa Renewable Energy Research Centre, the Director of Midea Electrical Machines and Control Systems Research Centres, and the Director of Sheffield CRRC Electric Drives Technology Research Centre. His current major research interests include the design and control of permanent magnet brushless machines and drives for applications ranging from electrified transportation through domestic appliance to renewable energy.

Dr. Zhu is the recipient of the 2019 IEEE Industry Applications Society Outstanding Achievement Award and the 2021 IEEE Nikola Tesla Award. He is a Fellow of the Royal Academy of Engineering and the IET, U.K.



Geraint Wyn Jewell received the B.Eng. and Ph.D. degrees in electrical engineering from The University of Sheffield, Sheffield, U.K., in 1988 and 1992, respectively.

Since 1994, he has been a Member of Academic Staff with the Department of Electronic and Electrical Engineering, The University of Sheffield, where he is currently a Professor of Electrical Engineering, the Head of the Department, and the Director of the Rolls-Royce University Technology Centre in Advanced Electrical Machines. He held an Engineering and Physical Sciences Research Council Advanced Research Fellowship from 2000 to 2005 and a Royal Society Industry Fellowship with Rolls-Royce from 2006 to 2008. His research interests include the modeling and design of a wide variety of electromagnetic devices, notably electrical machines for aerospace and high-temperature applications.



Jintao Chen (Senior Member, IEEE) received the B.Eng. and M.Sc. degrees from the Huazhong University of Science and Technology, Wuhan, China, in 2001 and 2004, respectively, and the Ph.D. degree from The University of Sheffield, Sheffield, U.K., in 2009, all in electrical engineering.

He is currently a General Manager with Midea Automotive Components Ltd., Hefei, China, and also with the Midea Shanghai Motors and Drives Research Center, Shanghai, China. His major research interests include the design of permanent magnet machines.



Liming Gong received the B.Eng. and M.Sc. degrees in electrical engineering from the Huazhong University of Science and Technology, Wuhan, China, in 2001 and 2004, respectively, and the Ph.D. degree in electrical and electronic engineering from The University of Sheffield, Sheffield, U.K., in 2012.

Since 2012, he has been with the Midea Welling Motor Technology (Shanghai) Co., Ltd., Shanghai, China. He is currently the General Manager with Servotronix Motion Control Company, Midea Group, Beijiaozhen, Foshan, China. His research interests include control of permanent magnet brushless machines and power electronics.



Di Wu received the M.Sc. degree in electrical engineering from the Huazhong University of Science and Technology, Wuhan, China, in 2011, and the Ph.D. degree in electronic and electrical engineering from The University of Sheffield, Sheffield, U.K., in 2015.

Since 2011, he has been working with the Midea Welling Motor Technology (Shanghai) Co., Ltd., Shanghai, China, and is currently the Head of Motor Development Department, Welling, Midea Group, Beijiaozhen, Foshan, China. His major research interests include the design and analysis of permanent magnet brushless machines.